Geothermics 89 (2021) 101931

Contents lists available at ScienceDirect

Geothermics

journal homepage: www.elsevier.com/locate/geothermics

Integrated Stress Field Estimation and Implications for Enhanced Geothermal System Development in Acoculco, Mexico

Michal Kruszewski[a,b], Hannes Hofmann[c], Fidel Gomez Alvarez[e], Caterina Bianco[d], Adrian Jimenez Haro[e], Victor Hugo Garduño[e], Domenico Liotta[d,f], Eugenio Trumpy[f], Andrea Brogi[d,f], Walter Wheeler[g], Eivind Bastesen[g], Francesco Parisio[h], Erik H. Saenger[i,a,b]

[a] Fraunhofer IEG, Bochum, Germany
[b] Ruhr University Bochum, Germany
[c] Helmholtz Centre Potsdam GFZ German Research Centre for Geosciences, Potsdam, Germany
[d] University of Bari Aldo Moro, Bari, Italy
[e] UMSNH Universidad Michoacana de San Nicolas de Hidalgo, Morelia, Mexico
[f] CNR National Research Council, Pisa, Italy
[g] NORCE, Bergen, Norway
[h] Chair of Soil Mechanics and Foundation Engineering, Technische Universitaet Bergakademie Freiberg, Freiberg, Germany
[i] Hochschule Bochum, Bochum, Germany

ARTICLE INFO

Keywords:
in-situ stress estimation
hydraulic stimulation
Enhanced Geothermal Systems (EGS)
Acoculco geothermal system
geothermal reservoir geomechanics

ABSTRACT

Data gathered from two geothermal exploration wells in the Acoculco caldera, within the Trans-Mexican Volcanic Belt, indicated that temperature is high enough for economic utilization, but permeability is insufficient. Hence, heat exploitation at this location may only be possible by Enhanced Geothermal System (EGS) technologies. To evaluate the potential for EGS development, a wide range of exploration work has been carried out in the framework of the international research project GEMex. In this manuscript, we present best estimates of the in-situ stress field conditions at the site – an important, yet highly uncertain, parameter for stimulation planning. The study is based on geological data, drilling parameters, geophysical logging, laboratory measurements on collected rock samples, and statistical analyses. The in-situ stress regime of the Acoculco geothermal area can be described as transtensional with a maximum horizontal stress striking in the NE-SW direction, a pore pressure gradient of 8.73 MPa·km^{-1}, a minimum horizontal stress gradient of 22.8 ± 3.3 MPa·km^{-1}, a vertical stress gradient of 24.3 ± 1.5 MPa·km^{-1}, and a maximum horizontal stress gradient of 42.9 ± 28.5 MPa·km^{-1}. Based on the predicted stress tensor, we estimate the maximum pressure required to enhance the rock permeability and discuss the potential EGS development options for the Acoculco geothermal area.

1. Introduction

The Acoculco field is located within the Trans-Mexican Volcanic Belt (TMVB) in the Puebla and Hidalgo states. The TMVB, stretching from WNW to ESE for about 1000 km, derives from a continuous, mainly calc-alkaline, volcanic activity, related to the NE-wards subduction of the Cocos and Rivera plates underneath the North America plate, along the Pacific margin (Demant 1978; Pasquare et al., 1991; Suter et al., 2001). The Acoculco geothermal area (Fig. 1), recognized by many authors as a caldera complex (De la Cruz and Castillo-Hernández, 1986; López-Hernández et al., 2009; Canet et al., 2010, 2015a), was studied by the Comision Federal de Electricidad (CFE). Two deep exploratory wells, EAC-1 and EAC-2, were drilled near surface manifestations, i.e., gas (predominantly CO_2) discharges and acid-sulfate springs (Canet et al., 2015b), in the Acoculco field.

The study area is located in the eastern sector of the TMVB (Fig. 1), a WNW-ESE oriented Neogene-Quaternary volcanic arc which crosses the central part of Mexico (Demant 1978; Pasquare et al., 1991; Gómez-Tuena et al., 2005, 2007; Ferrari et al., 2012). Since Pliocene, the present stress field in the study is characterized by the principal NNW-SSE trending extension (Pasquarè et al., 1988; Suter, 1991, Suter et al., 2001; Ego and Ansan, 2002; Ferrari et al., 2012; Dougherty and Clayton, 2014; Heidbach et al., 2016; García-Palomo et al., 2018). This overprints kinematics on structures associated with the ENE-WSW extension (e.g., the Mexican part of the North American plate Basin and Range) dominant from the mid-Miocene to the early Pliocene and giving rise to the southern termination of the Basin and Range structure of western North-America plate, developed under mainly the ENE-WSW trending extension faults (Pasquarè et al., 1988). The Acoculco volcanic system was developed in the 2.7 – 0.06 Ma period through the emission of domes, cinder cones, fissure lava flows, and ignimbrite eruptions (Avellán et al., 2019). The volcanic evolution of the study area was

https://doi.org/10.1016/j.geothermics.2020.101931
Received 5 March 2020; Received in revised form 15 June 2020; Accepted 10 July 2020
Available online 12 September 2020

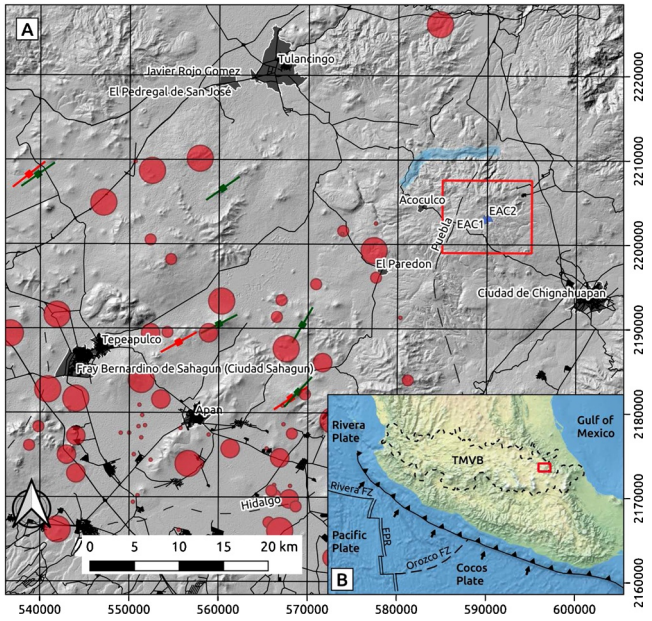

Fig. 1. A) The Acoculco caldera: shaded relief map of the Acoculco field with main villages and roads in the region; blue trace – Acoculco caldera rim; red markers – maximum horizontal stress direction indicators from the World Stress Map (Heidbach et al. 2016); green markers – maximum horizontal stress direction indicators from the Apan-Tezontepec scoria cones (García-Palomo et al., 2018); red dots – registered historical seismicity (between 1976 and 2017) with four bubble sizes representing event magnitudes (0.8 – 2.5, 2.5 – 3.0, 3.0 – 3.375, and 3.375 – 4.40) (García-Palomo et al., 2018); blue triangles – EAC-1 and EAC-2 wells; B) Distribution of the TMVB and regional tectonic setting through Central America; locations of the studied area are represented with red squares.

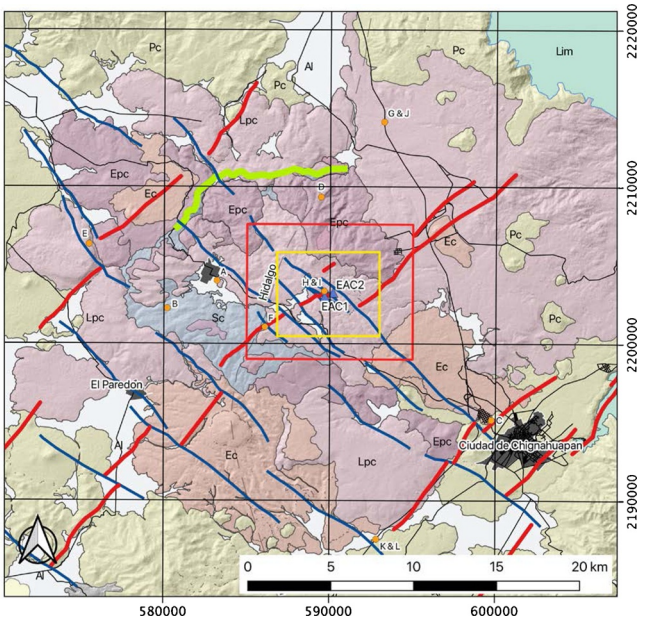

Fig. 2. Geological map of the Acoculco area after Sosa-Ceballos et al. (2018) with modifications: Al – Alluvial sediments, Ec – Extra-caldera volcanism (c.a. 0.90 – < 0.06 Ma), Lpc – Late post-caldera volcanism (c.a. 2.0 – 1.0 Ma), Epc – Early post-caldera volcanism (c.a. 2.6 – 2.2 Ma), Sc – Caldera-forming eruption (c.a. 2.7), Pc – Pre-caldera volcanism (c.a. 2.4 – 3.0 Ma), Lim – Limestone (Jurassic – Cretaceous); red rectangle – extent of the 3D geological model; yellow rectangle – location of the study area in Fig. 5B; blue solid lines – oblique to strike-slip faults; red solid lines – oblique to normal faults; green trace – Acoculco caldera rim; blue triangles – EAC-1 and EAC-2 wells; orange dots – locations of structural stations.

recently described by Sosa-Ceballos et al. (2018, and references therein), who divided the volcanic succession into pre-, syn- and post-caldera evolution, being the caldera formed during Pliocene-Pleistocene. The volcanic succession rests on the Jurassic-Cretaceous carbonate succession, deformed during the Laramide orogenesis (i.e., late Cretaceous-Oligocene). Regarding the fault arrays affecting the Acoculco area (Fig. 2), Avellán et al. (2019), and García-Palomo et al. (2018) indicate two regional fault systems, i.e., the NW- and NE-striking. From their studies, the NE-striking fault systems are characterized by a dominant normal component, whereas the NW-striking faults display an oblique component. A direct correlation between historical seismicity and fault systems in the Apan-Acoculco region was not found, although a NE-SW epicentral location trend was recognized (García-Palomo et al., 2018).

The Acoculco caldera, covering an area of 18 by 16 km, laying within the older and larger (32 km by diameter) Tulancingo caldera, was formed 2.7 Ma ago by an explosive eruption that triggered the collapse of the magma chamber roof and deposited about 127 km^3 of andesitic ignimbrite (García-Palomo et al., 2018; Sosa-Ceballos et al., 2018; Avellán et al., 2019). The volcanic evolution is divided into pre-, syn- and two post-caldera events, as indicated in Fig. 2, and recorded from the two (i.e., EAC-1 and EAC-2) exploration boreholes:

1 Pre-caldera events, which produced the emplacement of the Zacatlán-Chignahuapan basalt plateau (at least up to 200 m thick) and the formation of the Miocene pre-caldera domes and lavas (13 – 3 Ma) (Avellán et al., 2019).
2 Syn-caldera events, originating from two different periods of volcanic activity. The first ones, dated at 3.0 – 2.7 Ma, produced mostly dacitic to rhyodacitic lavas and pyroclastic deposits of up to 600 m thickness. The second event, 1.7 – 1.26 Ma aged, is referred to the formation of the inner Acoculco caldera and it generated up to 300 m of rhyolitic domes and ignimbrite deposits with minor dacite lava flows.
3 Post-caldera events, taking place after the Acoculco caldera collapse, when monogenetic volcanism developed, determining a large basaltic-andesite plateau (López-Hernández et al., 2009; Canet et al., 2010a).

The volcanic complex rests upon a Mesozoic carbonate sedimentary series composed mainly of Jurassic interbedded pelites, biopelites with minor limestones, and dolomites rich in hydrocarbons. On the top of this series calcarenites, reef limestones with minor pelites, and siltstone of late Cretaceous age lie in stratigraphic concordance. This basement was intruded by a late Mesozoic granitic body that caused the limestones to metamorphose into marbles (Canet et al., 2010a, and references therein). Whereas regionally these carbonates are kilometres thick, in the central area of the Acoculco caldera exploration wells were drilled through approximately 800 m of carbonate lithologies and met much younger 180 ka (Avellán et al., 2019) granitoids at depth of about 1600 m (Pulido et al., 2010).

Although the results from the two vertical exploration boreholes, i.e., EAC-1 drilled in 1995 to a total depth of 2000 m and EAC-2 drilled in 2008 to a total depth of 1900 m, indicate temperatures of up to 300 °C at the bottom hole depth of ~2 km, exploitable geothermal fluids were not discovered (Pulido et al., 2010; López-Hernández et al., 2009). The low permeability of rock formations encountered in Acoculco wells is expected to be related to two main factors. First, the intrinsic permeability of marbles, skarns, and granites is low, which may limit the development of the hydrothermal system from the very beginning. Second, the NW- and NE-striking regional faults, that may have channeled the ascent of magmatic and hydrothermal fluids, are partially sealed, due to the deposition of hydrothermal minerals (López-Hernández et al., 2009).

The Acoculco field is considered as potential Enhanced Geothermal System (EGS) site as a consequence of the high temperature and low

permeability. EGS technologies aim at improving the hydraulic performance of a geothermal system by hydraulic, thermal or chemical stimulation treatments (Gérard et al., 2006). While these technologies require detailed knowledge of the geology, hydrology, and rock properties, the in-situ stress field is one of the primary controls on stimulation results, particularly for hydraulic stimulation treatments. For example, hydraulic fractures open in the direction of least resistance (i.e., the minimum principal stress direction); the magnitude of the least principal stress (S_3) dictates the fracture opening and re-opening pressure of hydraulic fractures; vertical fracture growth can be contained by stress barriers, and the stress magnitudes and directions govern slip, stability, and opening of pre-existing fractures and faults (Zoback et al., 2007). Therefore, it is required to estimate the magnitudes and directions of the largest (S_1), intermediate (S_2), and least principal stresses, their variability with depth, and uncertainty.

Unfortunately, the available stress data in the Acoculco field is limited and no stress indicators are available in the vicinity of the planned location for the stimulation operation (Fig. 1). Additionally, the determination of in-situ principal stresses orientation and magnitude is a complex task, and uncertainty is bound to propagate into the predicted stimulations concepts. Therefore, we update the state of knowledge on the stress field near the EAC-1 and EAC-2 wells in the Acoculco area and highlight the uncertainties that remain by a statistical representation of the in-situ stress field. The study is based on the re-evaluation of existing data and new multidisciplinary exploration studies that were performed within the framework of the international research project GEMex[1] (2016 – 2020). Finally, we highlight further exploration options and demonstrate the influence of the in-situ stress tensor on the potential EGS site development concepts.

2. Methodology

2.1. Literature Studies

Literature documenting past studies on the Acoculco caldera served as the basis for this study. It included local geological studies, available wellbore information from both Acoulco wells (i.e., cuttings and core studies from EAC-1 and EAC-2 wells, recorded fluid losses, and lithology from the EAC-1 well) (Gama et al., 1995; Torres et al., 1995; Ramírez and García, 2006; Rocha et al., 2006; Contreras, 2008; Schlumberger 2008; Pulido et al., 2010), laboratory studies on samples from outcrops at Acoculco and Las Minas carried out within the GEMex project (Weydt et al., 2018, 2019; Lepillier and Bruhn, 2019), and stress indicators from the World Stress Map (Heidbach et al., 2016).

2.2. Geological Field Studies and 3D Geological Model

The collection of geological data in the field was based on the classical approach of structural geology, considering field mapping for the reconstruction of the geological body geometry, the orientation of foliations (attitude of bedding and fractures, including faults) and kinematic indicators on fault slip surfaces (pitch). The latter ones, integrated with the attitude of the faults, were used to reconstruct the paleo-stress field, assuming the maximum shear as parallel to the kinematic indicators after McKenzie (1969) and Angelier (1979).

The 3D geological model of Acoculco was implemented in the 3D GeoModeller package[2]. The methodology for setting up the model of the Acoculco caldera is described in detail in Calcagno et al. (2018). To build the 3D geometries the co-kriging interpolator was used. The 3D point located on the geological interfaces and the 3D vectors showing dips of these geological interfaces were used at the same time by the interpolator as input data (Lajaunie et al., 1997). The interpolation produces a 3D scalar potential field where isovalues represent geological interfaces. A geological pile describes the chronological and topological relations between the geological formations. It allows automatic management of the geological boundaries (gradual or erosional). The links between faults and formations were also described in the modelling process, to automatically compute how faults affect formations. When faults interact with each other, they are combined in a fault network to describe their relationship. The 3D geological model was built by taking into account the most updated geological map from Avellán et al. (2019), the lithology from the two available boreholes and geological fieldwork performed during the GEMex project, and two geological cross-sections extrapolated from the aforementioned geological map.

2.3. Analysis of Drilling and Logging Data

The public electricity provider of Mexico Comisión Federal de Electricidad (CFE) drilled two vertical exploration wells, i.e., EAC-1 in 1995 to a final depth of 2000 m and EAC-2 in 2008 to a final depth of 1900 m, in the Acoculco geothermal area. Parts of the drilling and logging data were made available to the authors and informed the analysis described in this manuscript. The provided data included:

1 Daily drilling reports from the EAC-2 exploratory well. From such reports information about applied drilling fluid densities, fluid pumping pressures, and drilling rates were acquired. This allowed computation of total wellbore pressures and help identify potentially fractured zones. Drilling reports provided information on the stress-related events such as steam influxes, which were used to confirm pore pressure predictions and drilling fluid losses which served as inputs for the estimation of S_3 component, and location of potential fracture zones. Information about Formation Integrity Tests (FIT), which were used as inputs for the S_3 prediction, were acquired also from drilling reports. Additionally, results from the cuttings studies were used to construct a detailed lithological profile of the EAC-2 well.
2 Geophysical logging data, including acoustic, gamma ray, resistivity, neutron density, caliper logs performed in the EAC-2 well with environmental corrections carried out by the logging contractor. From acoustic and neutron density logs, dynamic Poisson's ratio, and Young's modulus profiles were computed (Gardner et al., 1974). Additionally, unconfined compressive strength (*UCS*) for the logged interval was established using the correlation by Coates & Denoo (1981) based on bulk densities of rocks, acquired from neutron density log, and shear wave velocity and then compared with laboratory studies. Caliper log was used to investigate drilling conditions and provide information on borehole damage. Additionally, information about the grain and bulk density, total, and effective porosity and volumes of main mineral components from the EAC-2 well were acquired from the logging contractor. These results were used to characterize reservoir rocks. Available bulk densities were applied for the calibration of the vertical stress component in the Integrated Stress Model (ISM).
3 Temperature and pressure profiles from EAC-1 and EAC-2 wells, which were used to constrain the pore pressure gradient in the ISM and locate potential fracture zones.
4 Completion schemes of EAC-1 and EAC-2 wells used to select the appropriate stimulation concepts.

2.4. Integrated Stress Model (ISM)

The reevaluated and new stress information acquired throughout this study was used to develop ISM for the Acoculco geothermal area. Such model bundles all available stress information with theoretical

[1] http://www.gemex-h2020.eu (last access: 10 February 2020).
[2] https://www.geomodeller.com (last access: 27 January 2020).
[3] http://www.geo.cornell.edu/geology/faculty/RWA/progs/faultkin.html (last access: 8 June 2020).

assumptions, and statistical methods to provide the most realistic estimates of the currently acting in-situ stress tensor. Due to the limited amount of stress data in the Acoculco area and the large uncertainty of the stress state, we have employed the Monte Carlo (MC) simulation approach with defined input data distributions, integrated into the MATLAB script, to quantify the stress tensor and address its uncertainty.

To illustrate the stress conditions of the Acoculco field, and provide input data for the MC simulations, some reasonable stress boundaries had to be assessed. In extensional stress regimes, horizontal stresses may be significantly lower than the vertical stress, where the S_3 and S_2 will both be horizontal and S_1 the vertical stress. In more compressive stress regimes, both horizontal stress components may be greater than the vertical one (Anderson, 1951). Assuming the frictional equilibrium theory and vertical stress being the principal component, the ratio of effective principal stresses is equal to (Jaeger et al., 2016)

$$\frac{(S_1 - P_p)}{(S_3 - P_p)} = (\sqrt{\mu^2 + 1} + \mu)^2 \quad (1)$$

where μ is the friction coefficient of a pre-existing fault in-situ. Based on this theory, theoretical boundaries for minimum (S_{hmin}), and maximum horizontal stress (S_{Hmax}) can be established for a given stress regime provided that both pore pressure (P_p), and vertical stress (S_v) components are known.

A pressure profile, measured 312 hours after drilling operations ceased, from the EAC-1 well was assumed as P_p. Such conditions are considered to be the closest to the equilibrium state in-situ. Additionally, registered pressures of steam influx events, recorded in the EAC-2 well, were integrated into the P_p analysis.

One of the primary input values for the MC simulation is S_v. It can be relatively well constrained using bulk density measurements obtained either from laboratory tests on outcrop or reservoir samples or from geophysical logging. The bulk density data for this study was acquired from laboratory studies by Weydt et al. (2018, 2019), carried out within the GEMex project on analogue outcrop samples from the Acoculco and Las Minas sites. Bulk density of 962 ± 10 kg·m^{-3} was assumed for rhyolitic ignimbrite, 1941 ± 397 kg·m^{-3} for rhyodacite, 2297 ± 57 kg·m^{-3} for dacite, 2657 ± 42 kg·m^{-3} for limestone, 2690 ± 120 kg·m^{-3} for marble (based on analogue outcrop samples from Las Minas), 3360 ± 490 kg·m^{-3} for skarn (based on analogue outcrop samples from Las Minas), and 2640 ± 150 kg·m^{-3} for granite (based on analogue outcrop samples from Las Minas) with gravitational acceleration constant of 9.81 m·s^{-2}. We have utilized a normal distribution of bulk density values as inputs for the MC simulations. Results from density logging in the EAC-2 well were used to cross-check the accuracy of S_v computations.

Results of FIT at depths between 330 and 1830 m in the EAC-2 well, were used to constrain the magnitude of S_3. FIT's were carried out on specific occasions (i.e., pipe sticking at 330 m depth, and trapping of the casing pipe during casing installation at depth between 770 and 800 m) during drilling and completion operations in the EAC-2 well. In case of these events, forced cementation had to be carried out, and FIT's had to be performed to ensure that rock fracturing will not be induced during drilling of the next wellbore section, and the well will be safely controlled in a case of a blow-out. The FIT's at greater depths (i.e., > 800 m) were performed at the end of drilling operations, during the cleaning of the well from the residues of the drilling mud with a water-lignite solution. During the FIT, pressure in the well was increased to a pre-determined value. When during FIT no fluid leak-off was observed it was assumed that S_3 value is higher than the sum of pressure exerted by the fluid column in the well (for simplicity, density of working fluid during FIT of 1000 kg·m^{-3} was assumed) and the applied differential pressure (*dP*). In a situation when a naturally permeable fracture exists at depth, leak-off will occur as soon as pumping starts. No additional (e.g., image log) measurements were available from the EAC-2 well, thus information about the pre-existing fractures within the tested intervals could not be assessed. The complexity of carrying out any type of in-situ hydraulic stress measurement or advance borehole logging increases significantly with increasing temperatures at depth. If leak-off was observed, it was assumed that a hydraulic fracture developed, or a pre-existing fracture opened (i.e., shearing was initiated). Thus, the sum of pressure exerted by the fluid column in the well and *dP,* being maximum pressure at the wellhead applied during a FIT, serves as a lower bound on the S_3 magnitude in the MC simulations within the tested depth interval with an assumption of no pre-existing fractures. For both normal and strike-slip faulting regimes maximum magnitude of S_{hmin} cannot exceed S_v. Therefore, the S_v magnitude was used as an upper bound of S_3.

Drilling fluid losses are the result of the applied total wellbore pressure (P_w) exceeding S_3 in the open hole section, leading to its tensile failure. This assumption, alternatively to the FIT results, allows assessing S_3 at intervals of fluid loss, assuming that no pre-existing fractures were encountered during drilling operations. Such an assumption is considered as valid for the case of the Acoculco area, which, as mentioned before, is considered as a low permeability system. The total wellbore pressure, during fluid loss, was computed as a sum of the hydrostatic pressure column of the drilling fluid (P_{df}) and 95 % of the pumping pressure (P_s) at the well surface, assuming small pressure loss of 5 %, as presented in equation 2 (Brudy et al., 1997). This is justified by the fact that in Acoculco thixotropic drilling mud was used. During pump start, this type of drilling mud transfers the first pressure peak down the well with very small pressure loss. A different case occurs during mud circulation when larger dynamic pressure losses lead to lower P_w. As in this case study, we are interested only in the peak pressure experienced by the formation rock during drilling, thus pressure peak at the start of pumping with a pressure loss of only 5 % was applied. Surface pumping pressure and density of drilling fluid were assumed as an average of values registered during the day of the operation.

$$P_w = 0.95 \bullet P_s + P_{df} \quad (2)$$

S_{Hmax} is the stress component affected by the highest uncertainty. This is mainly due to the lack of available calibration data, such as borehole deformation observations, which is also the case in our study. The lower bound on S_{Hmax} magnitude in normal or strike-slip faulting regimes is equal to S_{hmin}. This constraint served as the lower bound on S_{Hmax}. For the computations of the upper bound on S_{Hmax} value, a strike-slip faulting regime was assumed based on the results from the geological fieldwork carried out within this study. The resultant equation for S_{Hmax}, assuming S_v being a principal component and frictional equilibrium theory, the upper bound on S_{Hmax} will amount to

$$S_{Hmax} = [(S_{hmin} - P_p) \bullet (\sqrt{\mu^2 + 1} + \mu)^2] + P_p \quad (3)$$

A uniform distribution of μ between the value of 0.6 and 0.85 was assumed. The lower bound is based on the observation that faults may have friction coefficients of 0.6, or lower, depending on the fault gauge mineralogy (Zoback et al., 2007). The upper bound is based on laboratory experiments on fractures reported by Byerlee (1978), who propose a value of 0.85 for normal stresses below 200 MPa.

Based on the estimated values of the principal in-situ stresses, maximum pressures required for hydraulic fracturing (i.e., formation breakdown pressure, *FBP*) can be calculated at potential stimulation targets for a case of a vertical well assuming apparent tensile rock mass strength being equal to the uniaxial tensile strength, T_0, no leak-off, and no poroelastic effects (Amadei and Stephansson, 1997)

$$FBP \leq 3S_{hmin} - S_{Hmax} - P_p + T_0 \quad (4)$$

Such criterion gives an upper bound on the effective stimulation pressure (or overpressure) required to hydraulically fracture formation rock at specific depth in-situ. The actual stimulation pressure in wells such as those in the Acoculco area, will be, most likely, much less than

FBP due to the irregular wellbore shape and potentially pre-existing natural fractures. Therefore, pressure computed from Equation 4 should be regarded as a maximum surface treatment pressure (neglecting pressure losses), as it will most likely greatly overestimate the pumping pressure during actual stimulation. The experience with stimulation of crystalline rock at numerous sites suggests that the pressure at depth reaches but rarely significantly exceeds S_3 during hydraulic stimulation (McClure and Horne, 2014). The maximum treatment pressure, however, dictates the required equipment for performing hydraulic stimulation with chemical, thermal, and hydraulic shear stimulations operating below such pressure. Results of T_0 from laboratory tests on outcrop samples from the Acoculco site by Lepillier and Bruhn (2019), and studies by Barahim et al. (2017), Kallu & Roghanchi (2015), and Karaman et al. (2015) were applied. T_0 of 6.3 ± 2.7 MPa was assumed for rhyolitic ignimbrite, 18.2 ± 8 MPa for rhyodacite, 10.7 ± 5.5 MPa for dacite, 15 ± 4.3 MPa for limestone, 11 ± 2 MPa for marble, 14 ± 6 MPa for skarn, and 14 ± 0.5 MPa for granite. Log-normal distribution of T_0 for MC simulations was assumed. Thermal stresses were not considered in computations of the in-situ stress tensor, due to the vicinity of the wellbore being significantly cooled down by an extensive fluid circulation during drilling operations. A total amount of 10^4 realizations in the MC simulations, allowed to extract the statistical distribution of the three principal in-situ stress components and stimulation pressures with their uncertainties, and variations with depth.

3. Stress Indicators

3.1. World Stress Map Data

Information on S_{Hmax} direction was extracted from the World Stress Map (WSM) database (Heidbach et al., 2016). Three measurements of S_{Hmax} azimuth are available at 44, 32, and 27 km distance from the Acoculco site. All of them are based on studies of volcanic vent alignments of Quaternary age (represented with red markers in Fig. 1). The three measurements are consistent, with S_{Hmax} azimuth of N52 °E, N56 °E, and N61 °E, based on 7, 5, and 12 data points. The measurements indicate the presence of a normal faulting stress regime. The stress indicators are of good quality (category B). No records of stress magnitudes are available for the mentioned measurements from the WSM database. The regional S_{Hmax} direction is, thus, estimated to strike NE-SW.

3.2. Geological Data

Stress field determinations were also derived from the kinematic analysis of fault surface data from faults exposed in the Acoculco area. Fieldwork data (Fig. 2 and Fig. 3) indicate that the tectonic depressions where Quaternary continental and volcanoclastic sediments accumulated are bounded by up to 12 km long the NE-striking faults, dipping 70 – 80° towards NW, with length up to 12 km. These tectonic depressions are also delimited by NW-striking fault segments, typically 10 km long, overstepping each other and associated with NW-trending brittle shear zones, up to about 3 km width. Thus, a coeval fault activity during the Quaternary is suggested for the NE- and NW-striking systems, implying a common origin in the same stress field. This is also supported by the Quaternary age of the volcanic manifestations at the surface and their spatial distribution: volcanoes are aligned both along the NW-and NE-striking faults, and/or are located at the intersections between the two fault systems (García-Palomo et al., 2018; Avellán et al., 2019).

The structural and kinematic collection of fault-related data was carried out through structural stations, generally located along the main regional faults (Fig. 2). Observations and data analysis are from the minor faults (Fig. 3) associated with the master faults shown in Fig. 2. With this limitation, independent of their orientation, the bulk of the meso-faults affecting the Volcanites are characterized by apparent offsets of a few meters and a fault-damage zone up to 50 cm. A minor dataset is from the fluvio-lacustrine sediments, where although the apparent offset is in the order of a few dm, the displacement is younger than 12 ka. These faults are characterized by a thin core, up to 5 cm, and their fault damage zone width is in the order of 10 – 15 cm.

A few major faults have been mapped on the surface and display a well-developed fault core and damage zone. One example is exposed several hundred meters from the Acoculco wells (Fig. 4A; Structural station A13, Fig. 5B). This fault is a NE-SW trending normal fault with a damage zone associated with the vein mineralization of opaline quartz. Two NW-SE transfer faults are cutting this normal fault (Fig. 4B; Fig. 5B). Although these are not continuously exposed, kinematics on associated minor faults, the occurrence of seismites (i.e., earthquake-related deformation) in the fluvial-lacustrine sediments and the alignment of pockmarks and gas seeps support the presence of these transfer structures. Another location about 10 km north of the borehole site displays major faulting in andesites and basalt equivalent to deeper units in the Acoculco wells (i.e., Volcanites). The fault zone consists of at least two faults with a narrow 1 m thick cataclasite zone (fault core) with an oblique dextral shear sense. A dominant set of N-S trending clustered joints with alteration and iron oxide (in cases sulphur) mineralization are apparent in the damage zone between the faults and on the sides. Apart from these structures, faults with larger apparent offsets and damage zones have rarely been recognized at the outcrop scale. Associated with faults, a well-organized fracture network is occasionally visible, defining an exposed domain up to 10 m (Fig. 3A-G).

Kinematic indicators are given by slickenlines and grooves (Fig. 3H-L). When these were not accompanied by other structures indicating the direction of movement (i.e., steps and Riedel fractures), the dislocation of marker levels was the key factor to obtain a complete kinematic picture. In the absence of such indicators, slickenlines were not included in the dataset. The orientation of the meso-faults is consistent with the regional-scale structures (Fig. 3M-R), thus displaying the NW- and NE-striking fault systems. Kinematic indicators of the NW-striking fault system in some cases show two clearly superposed movements (Fig. 3L). The first movement is defined by right-lateral strike-slip to moderately-oblique-slip movements (Fig. 3H, J, K), while the second movement is characterized by a clear vertical component, even if a right-lateral minor component remains present. In contrast, the NE-striking faults maintain a dominant vertical component (Fig. 3I) even when different kinematic indicators were recognized on their fault-slip surfaces. Since kinematic relationships are already clear in the field, statistical approaches to relate striations to different paleo-stress fields (e.g., Sippel et al., 2009 with references therein) are not necessary, assuming that the measured slickelines are parallel to the main shear stress. In this view, kinematic and geometrical data from fault surfaces can be used to carry out paleo-stress analysis, graphically represented by double-couple fault-plane solution diagrams. In Fig. 3 the obtained fault plane solutions are plotted in the lower row of stereonets, following the fault-trends and their dominant kinematics. Two different focal mechanisms are therefore reconstructed for the NW-striking faults, respectively related to the first (Fig. 3M, P) and second (Fig. 3N, Q) kinematic events. Since it was not possible to differentiate the kinematic events on the NE-trending faults, these are reported in the same diagram (Fig. 3O, R).

The focal mechanism, indicating a transcurrent component (Fig. 3P), shows a regional NNW-stretching direction, compatible with previous knowledge (e.g., Avellán et al., 2019). This extensional direction can also explain the geometry and kinematics of the NE-striking normal faults, during the first kinematic event. In this framework, the NW-trending structures played the role of transfer faults. To explain the second kinematic event (i.e., the focal mechanism given in Fig. 3Q), the regional uplift is considered. If vertical movements are dominant, then all pre-existing structures are characterized by dominant vertical movements (Fig. 3Q, R). The different kinematics and geometry of faults can be explained in the same tectonic extensional context, under

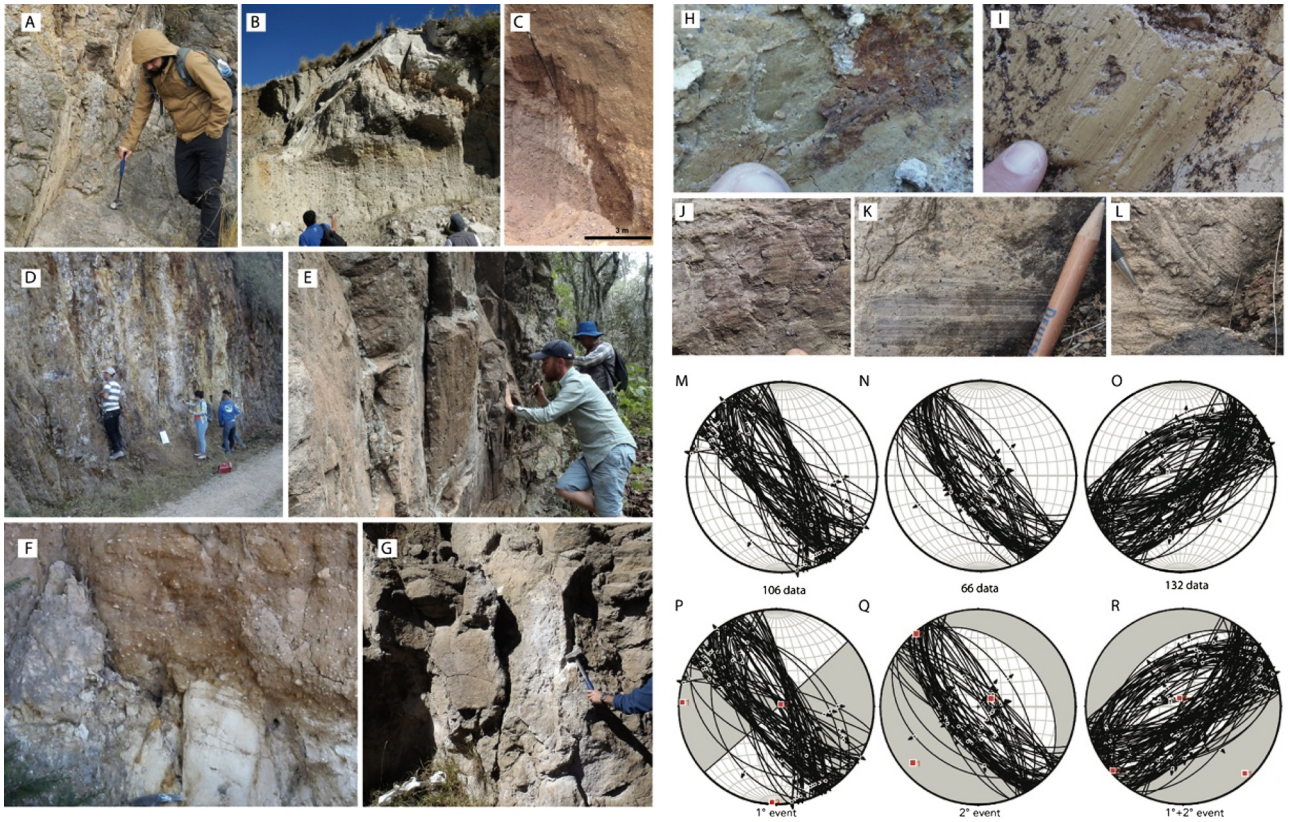

Fig. 3. Examples of meso-faults at a different scale of observation from the study area: A) normal fault in Quaternary andesitic lavas, displaying a clear fault-surface; B) system of normal faults in Quaternary ignimbrite; C) normal fault in Quaternary scoriae-deposits; D) system of meso-faults accompanying the main NW-trending structure; E) damage zone in an NW-striking fault; F) faults affecting the soil; G) fault-damage zone in Pliocene lavas. Locations of outcrops are given in Fig. 2; Examples of kinematic indicators on fault-slip surfaces: H) slickenlines from fault affecting Quaternary lacustrine sediments; I) slickenlines developed during sulfur-rich fluid circulation; C) and D) examples of transcurrent movements on the NW-striking faults; J) two generations of slickenlines: the ones with a dominant normal component are overprinting the transcurrent ones, on the NW-striking faults; M) and N) stereonets (equal angle, lower hemisphere projection) summarizing the transcurrent to oblique and normal kinematics on the NW-striking faults, respectively O) stereonets summarizing the normal kinematics on the NE-striking faults; P), Q) and R) focal mechanisms from the fault dataset given in M), N) and O), respectively. Inversion of fault data was performed with FaultKin[3] software.

the same stress field, characterized by a dominant NW-trending extensional direction. The kinematics of the faults in the Acoculco area is, therefore, a consequence of the competition between crustal stretching and regional uplift. When stretching is dominant, the NW-trending structures are transfer faults, coeval with the NE-trending normal faults; when uplift is dominant, all the pre-existing structures played the role of normal faults, thus explaining the overlap of kinematic indicators on the NW-trending fault-slip planes.

A large amount of structural data collected in the GEMex project in conjunction with the geological map from Avellán et al. (2019) and the geological description of both Acoculco wells, allowed the construction of a local 3D geological model with horizontal dimensions of 8.5 km by 10.5 km and depth of 10 km. The model reproduces the structural setting in a 3D space, in the surrounding of wells, highlighting the different kinematics of the two sets of faults (Fig. 5).

3.3. Drilling Data

The first exploratory well, EAC-1, was drilled between 12 February and 25 May 1995 to investigate the geothermal potential of the Acoculco reservoir for electricity production. EAC-1 is a vertical, 2000 m deep well, completed with 6 ” open hole section from 800 to 1500 m and a 5 7/8 ” open hole section from 1500 m down to the total depth (Appendix A). Drilling has revealed scant reservoir permeability with all fluid losses during drilling being smaller than 10 $m^3 h^{-1}$. Small drilling fluid losses were encountered at depths of 1369 m (2.0 $m^3 h^{-1}$), 1736 m (6.4 $m^3 h^{-1}$), and between 1909 and 1918 m (1.5 $m^3 h^{-1}$) (Ramírez and García, 2006). At a shallow depth of 70 m, the well encountered a permeable zone that discharged a large quantity of gas (Gama et al., 1995). Linear temperature profiles registered in the EAC-1 well indicate conductive thermal regime with possible convective zones identified as thermal anomalies at depths of 1250 m and 1650 m (Pulido et al., 2010). Analysis of core samples from the EAC-1 well by Rocha et al. (2006) showed fractures with 37º, 80º, 84º, 75º, 70º, and 74º dips measured relative to the core and stratal dips of 48º, 54º, 50º, 56º, and 45º. From the studies performed by Gama et al. (1995), intensive fracturing was reported at depths between 300 and 303 m, with all fractures being filled with calcite. At depths between 600 and 603 m, a sealed fracture was detected. Multiple calcite- and pyrite-filled fractures were observed between 850 and 853 m depth. Rock formations penetrated by the EAC-1 well are composed of vitric tuffs, dacites, ignimbrites, rhyodacites, skarns, marbles, aplites, and granites (Torres et al., 1995; Contreras 2008) (Fig. 6).

The second well in the Acoculco field, EAC-2, was drilled between 1 May 2008 and 17 November 2008 to a final depth of 1900 m in a lateral distance of around 500 m from the EAC-1 borehole. The well is vertical and completed with a 5 7/8 ” open hole section from the depth of 800 m down to the well bottom (Appendix B). Drilling operations took 201 days and more than 50 drill bits were used to reach the final target. The well was drilled with an overbalanced technique with drilling fluid density between 1.04 and 1.28 $g{\cdot}cm^{-3}$. Similarly, to the results from the EAC-1 well, temperature profiles in the EAC-2 well indicated a conductive thermal regime. Formations penetrated during drilling were composed of rhyolitic ignimbrite, rhyodacite, dacite, limestone, marble,

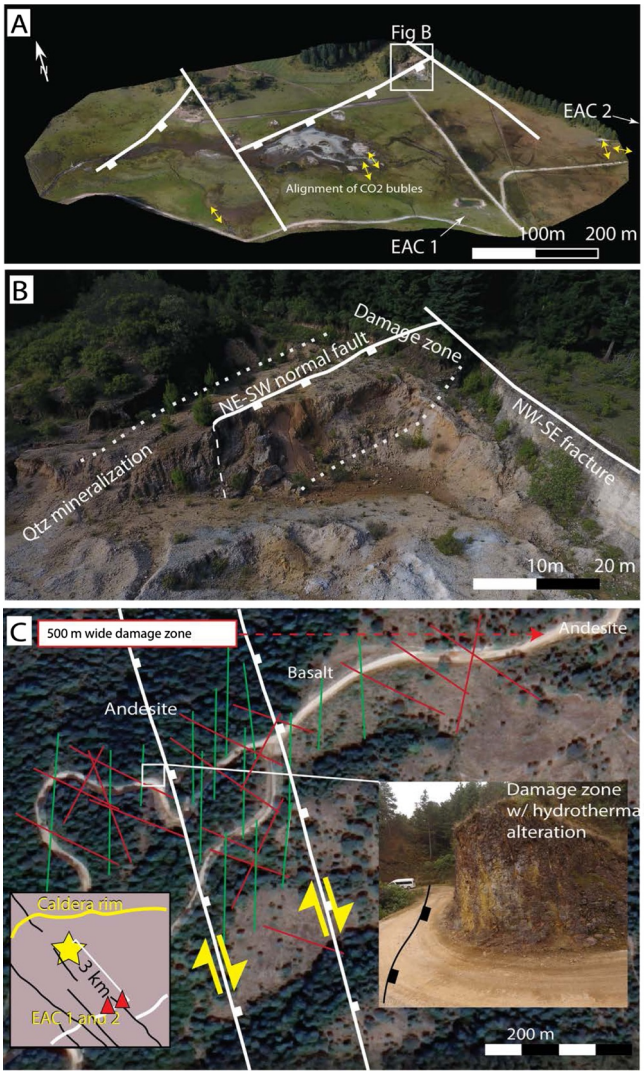

Fig. 4. Major outcropping faults in the Acoculco caldera; A) Overview of faults near EAC wells, screenshot from a 3D outcrop model (faults are mapped based on high-resolution terrain model and extrapolated to exposed segments). Yellow arrows indicate the alignment of bubbles in the spring lakes, oriented parallel to the NW-SE trending faults. Faults are mapped as lineaments form the high-resolution terrain model generated from the drone imagery (location labeled as H & I in Fig. 2); B) Close up of the NE-SW and NW-SW-trending fault segments near the EAC wells (see Fig. 2 for the location). The NE-SW trending fault is associated with significant quartz cementation; it is assumed that this zone is tight regarding fluid flow; C) Outcrop approximately 3 km northwest of the EAC wells (location labeled as D in Fig. 2). The outcrop displays a major NW-SE trending oblique-slip fault zone with a wide and well-developed damage zone in pre-caldera lava flows (andesites and basalt). Hydrothermal alteration is observed along the fault zone. For fracture frequencies see the pre-caldera section in Fig. 10.

skarn, and granite (Schlumberger 2008).

Analysis of cuttings from the EAC-2 well carried out by Pulido et al. (2010) showed several partially sealed fractures at the intervals between 1520 and 1560 m. At the interval between 1570 and 1900 m, open fractures with the presence of epidote crystals were observed. Additionally, evidence of a fault between 1828 and 1842 m filled with quartz, euhedral pyrite, and well-developed epidote crystals was detected. Between 1834 and 1836 m intersection of two left-lateral faults is speculated (Pulido et al., 2010).

Fig. 7 presents the drilling data acquired from the EAC-2 well. In the logged interval, borehole diameter was much larger than the drill bit (represented with a red solid line in Fig. 7B), due to the multiple reaming operations carried out during drilling. These reamed intervals potentially led to large wash-out zones. Moderate rates of penetration (*ROP*) of 3 $m \cdot h^{-1}$ and more, were registered for the first 360 meters. Below this point, drilling speed remained low (i.e., < 2 $m \cdot h^{-1}$) and decreased further with depth. Below 360 m, applied drilling fluid density was 1.1 $g \cdot cm^{-3}$, between depths of 360 and 800 m density was increased to 1.3 $g \cdot cm^{-3}$, between 800 and 1600 m it was lowered to 1.2 $g \cdot cm^{-3}$, and from 1600 m until the well bottom it was again decreased to 1.1 $g \cdot cm^{-3}$.

Although most penetrated rock formations in the EAC-2 well were drilled without major circulation losses, small fluid losses were recorded at depths of 102 m, 337 – 388 m, 469 – 473 m, 803 m, and between 1839 – 1842 m. Linear temperature profiles registered in the EAC-2 well indicate, similarly to the EAC-1 well, a conductive thermal regime. Temperature profiles recorded between 6 and 24 hours after drilling ceased show a small heating-up zone at the last 100 m of the well. Differences between logged temperature profiles exist also at the first 400 m, where fluid losses were observed. This proves that the most permeable zones are located within the upper 400 m. Additionally, small fluid inflow zones are potentially located at depths of approximately 1050 m, 1300 m, 1550 m, and 1800 m based on anomalies located from temperature profiles.

Two major events of steam discharge were observed in the EAC-2 well during drilling. In the first one, at 333.2 m depth, the discharge pressure of 3.4 MPa was recorded. The blow-out was mitigated using six cement plugs. The second steam influx was recorded at 798.85 m depth with H_2S content between 20 and 295 ppm, CO content between 40 and 520 ppm, and discharge pressure of 4.8 MPa. During drilling of the EAC-2 well, 28 FIT's were carried out at various depths between 333 and 1830 m. Unfortunately, information on the test results, extracted from the drilling reports, was very limited and an indication of leak-off was often inconclusive. From the analyzed data, in only 7 tests leak-off was potentially observed, in 11 tests no leak-off was observed, and results from 10 tests remain inconclusive (i.e., available data is too scarce to decide if leak-off occurred). Leak-off was observed only in FIT's performed in the upper sections of the well (i.e., < 800 m). In the FIT measurements carried out within the greater well depths (i.e., > 800 m) during flushing operations, no acceptance of fluid was observed, and well was considered as impermeable.

3.4. Logging Data

On the 26 September 2008 acoustic logging was carried out in the open hole section of the EAC-2 well between depths of 785 and 1485 m (Schlumberger 2008). The quality of measurements was regarded by the logging contractor as good. On 13 November 2008, additional borehole logging, including gamma ray, neutron density, and resistivity logs, was carried out in the open hole section, between depths of 803 and 1394 m, primarily to investigate petrophysical properties of the Acoculco reservoir (Schlumberger 2008). The density of fluid used for borehole logging was 1.02 $g \cdot cm^{-3}$ and the maximum temperature registered during logging was 198 °C. Unfortunately, the logging tool was not run to the total depth of the well due to electrical failure of the logging cable. Fig. 8 presents results of both logging campaigns, covering the depths of skarns and marbles.

Based on the results of the logging campaign, a classification of the main mineral components into three major groups was carried out by the logging contractor. These groups included clays, quartz-feldspars-micas (Q-F-M), and igneous rocks. The main constituent in the logged interval are igneous rocks, with a minor volume quantity of Q-F-M and clays, of likely hydrothermal origin. Within the Q-F-M group the main constituent is likely to be quartz and to a lesser extent potassium feldspars (orthoclase) and muscovite as an accessory mineral. Such interpretation of the borehole logging results is in apparent conflict with presented cuttings-based lithology presented in Fig. 7, and it likely reflects not minerals from igneous rocks but high-temperature silicic alteration typical of skarns, such as garnets, amphiboles, and epidotes.

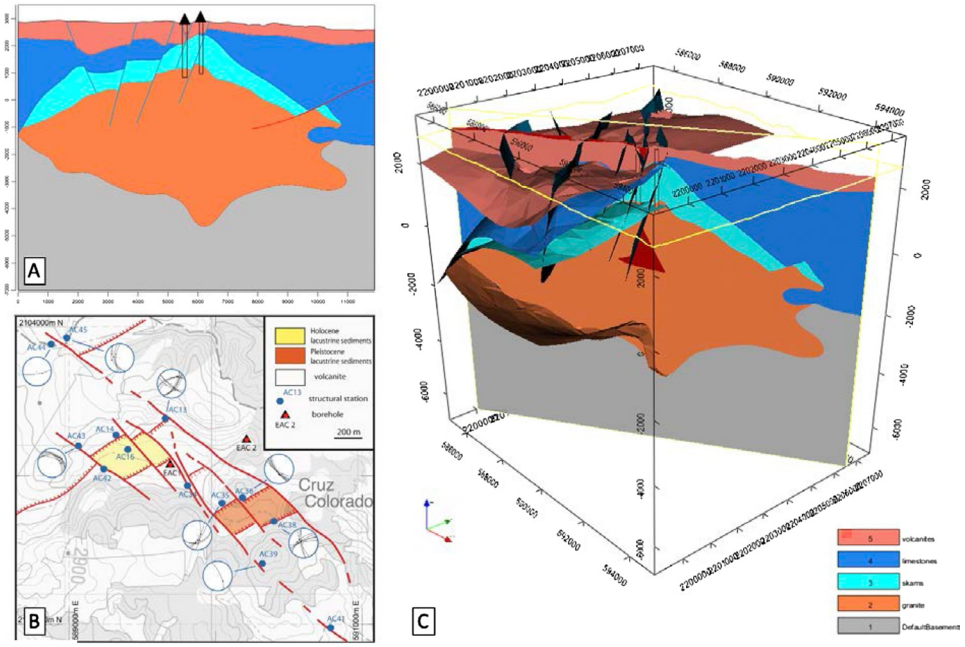

Fig. 5. A) A cross-section from the 3D geological model with main lithologies and Acoculco boreholes; B) structural map of the area surrounding Acoculco boreholes (faults, indicated by stereonets, are inferred to be active since they cut or bound sedimentary basins of very young age) represented by a yellow rectangle in Fig. 2; C) 3D representation of the Acoculco reservoir (strike-slip faults in blue and normal faults in red; extent of the geological model represented with a red rectangle in Fig. 2).

Borehole logging results indicate that formation rocks (i.e., skarns and marbles) have very low to absent porosity (i.e., < 5 %) and, as a result, potentially low matrix permeability. The acoustic and neutron density logs confirm this phenomenon, showing high V_p and high ρ_b. The *UCS* values predicted from borehole logging data, resulted in a value of 85.3 ± 28.9 MPa for skarns and 90.5 ± 29.6 MPa for marbles. Such values stay in relative agreement with the laboratory tests of *UCS* carried out by Lepillier and Bruhn (2019) on samples from the Acoculco field with resultant values of 119.6 ± 54.3 MPa for skarns and 136 ± 34.5 MPa for marbles.

4. Integrated Stress Model (ISM) Results

By integrating all available data and new measurements, the best estimate of the current in-situ stress field was derived including its uncertainties and variations with depth. This was done using the MC statistical approach, which results are presented in Fig. 9. The computed linearized P_p gradient amounted to the value of 8.73 MPa·km^{-1}. Discharge pressures of the two steam events follow closely the predicted P_p gradient. The average linearized S_v gradient, based on the bulk densities obtained from laboratory studies, amounted to 24.3 ± 1.5 MPa·km^{-1}. Such value follows closely the magnitude of S_v computed from bulk densities acquired from the geophysical logging in the EAC-2 well. The lower bound on the S_{hmin} magnitude was constrained based on the FIT's, where leak-off was observed (disregarding inconclusive FIT's and ones without leak-off), and P_w at fluid loss zones. The upper bound on S_{hmin} was considered as the value of S_v. It is observed that all values of the lower bound on S_{hmin}, i.e., from FIT's and

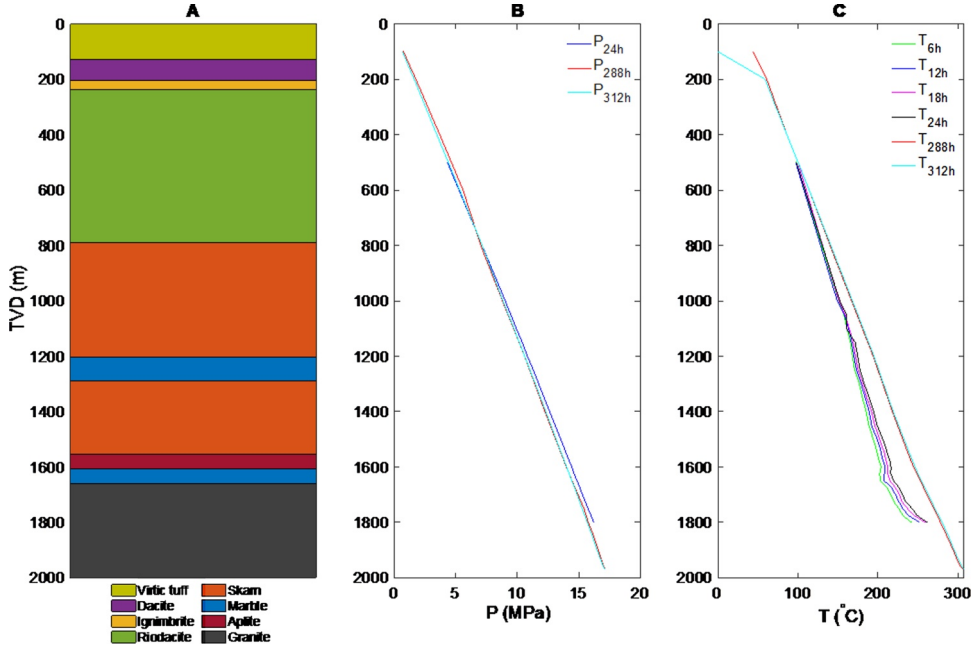

Fig. 6. Results from the EAC-1 drilling operations: A) lithology (adapted from Torres et al., 1995); B) pressure profiles registered with wire-line pressure gauge tool with a well being filled with fluid after drilling operation ceased; C) temperature profiles registered after drilling operation ceased (TVD – True Vertical Depth).

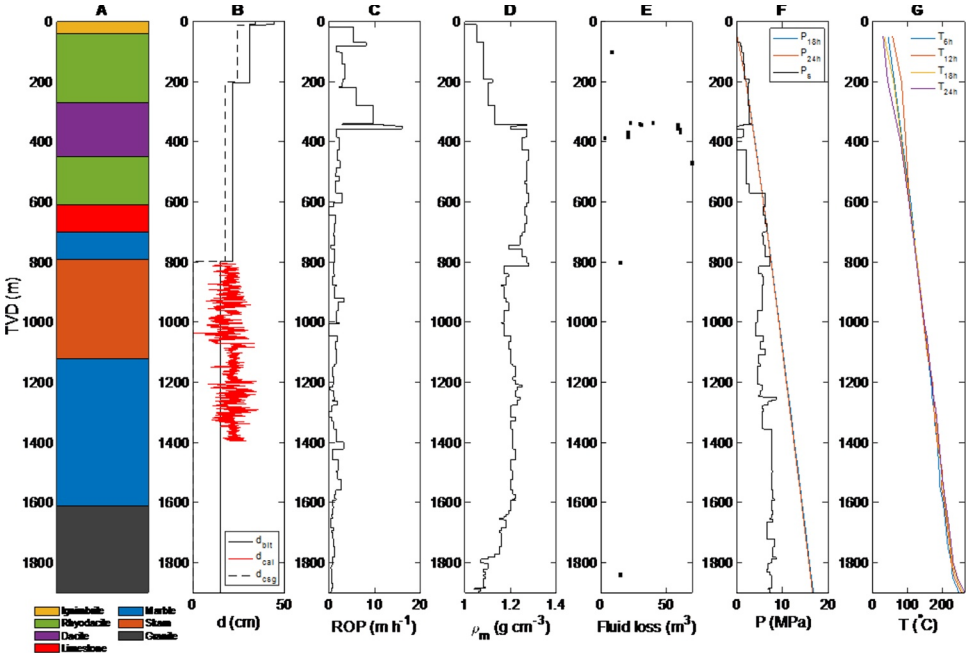

Fig. 7. Results from the EAC-2 drilling operations: A) lithology (based on cuttings); B) casing (d_{csg}), and drill bit (d_{bit}) diameters with results from a caliper log (d_{cal}); C) rate of penetration (*ROP*); D) density of the drilling fluid; E) recorded fluid losses during drilling; F) pressure profiles registered with wire-line pressure gauge tool with a well being filled with fluid after drilling operation ceased with surface pressures (P_s) applied during drilling; G) temperature profiles registered after drilling operation ceased.

fluid loss analysis, stay below S_v, which implicates either normal or strike-slip faulting stress regime, and which was also indicated by the geological fieldwork carried out within this study. Based on the MC simulations, the estimated average linearized gradient of S_{hmin} resulted in 22.8 ± 3.3 MPa·km^{-1}. As discussed previously, the greatest uncertainty exists always for the magnitude of S_{Hmax}. From our analysis, the average linearized gradient of S_{Hmax} amounted to 42.9 ± 28.5 MPa·km^{-1}. The high uncertainty of S_{Hmax} predictions can be seen in the probability density histogram of the mean principal stresses and *FBP* for a depth of 1830 m, a possible stimulation target (Fig. 9K). As a result of the insufficiently constrained magnitude of S_{Hmax}, predicted *FBP* also exhibit high uncertainties, that can range from relatively small overpressure to an extremely high overpressure exceeding 100 MPa at a potential simulation target depth of 1830 m.

5. Implications for Enhanced Geothermal System Development

Based on the limited data, we provide, the best estimate for the in-situ stress field within the Acoculco area. Especially the large uncertainty regarding the estimation of the S_{Hmax} magnitude warrants further measurements, such as borehole image logs, caliper logs, and (extended) leak-off tests, to improve the understanding of the in-situ stress field. This would reduce the uncertainties associated with stimulation measures of the two Acoculco wells and drilling of new wells in the area. We estimated the maximum expected overpressure required to fracture the rock, which is necessary to plan the hydraulic stimulation treatments. Due to the large uncertainties associated with the current stress field estimates, we did not calculate more detailed estimates of the *FBP* of hydraulic fracturing treatments or fracture/fault activation pressures for hydraulic shear stimulation treatments.

Both wells were potentially damaged during overbalanced drilling

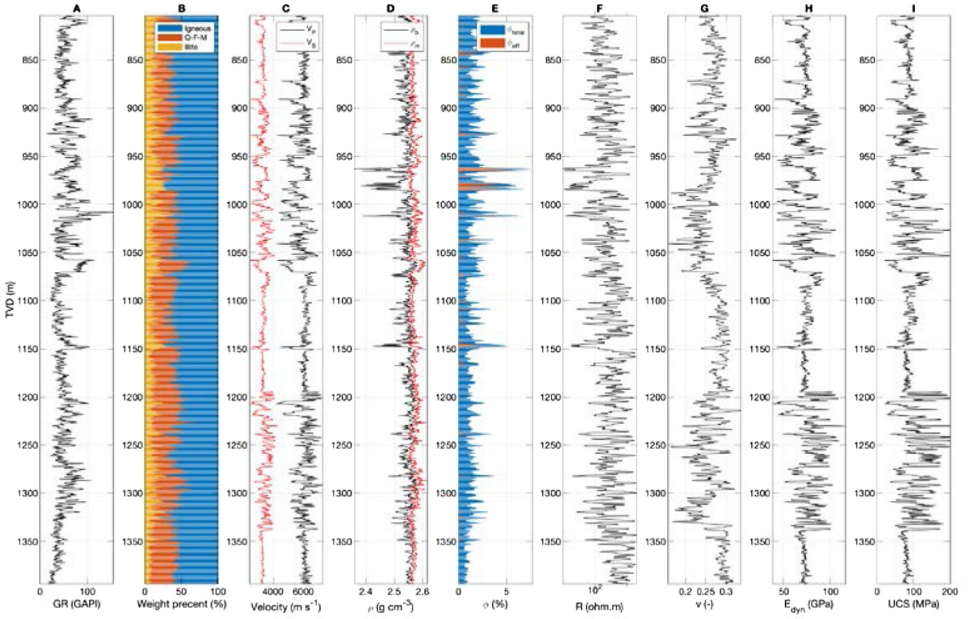

Fig. 8. Results of the borehole logging campaigns in the EAC-2 well: A) gamma ray (*GR*); B) main mineral components; C) compressional (V_p) and shear (V_s) wave velocities; D) bulk (ρ_b) and grain (ρ_m) density; E) total (ϕ_{total}) and effective (ϕ_{eff}) porosities; F) resistivity (*R*); G) dynamic Poisson's ratio (ν); H) dynamic Young's modulus (E_{dyn}); I) unconfined compressive strength (*UCS*).

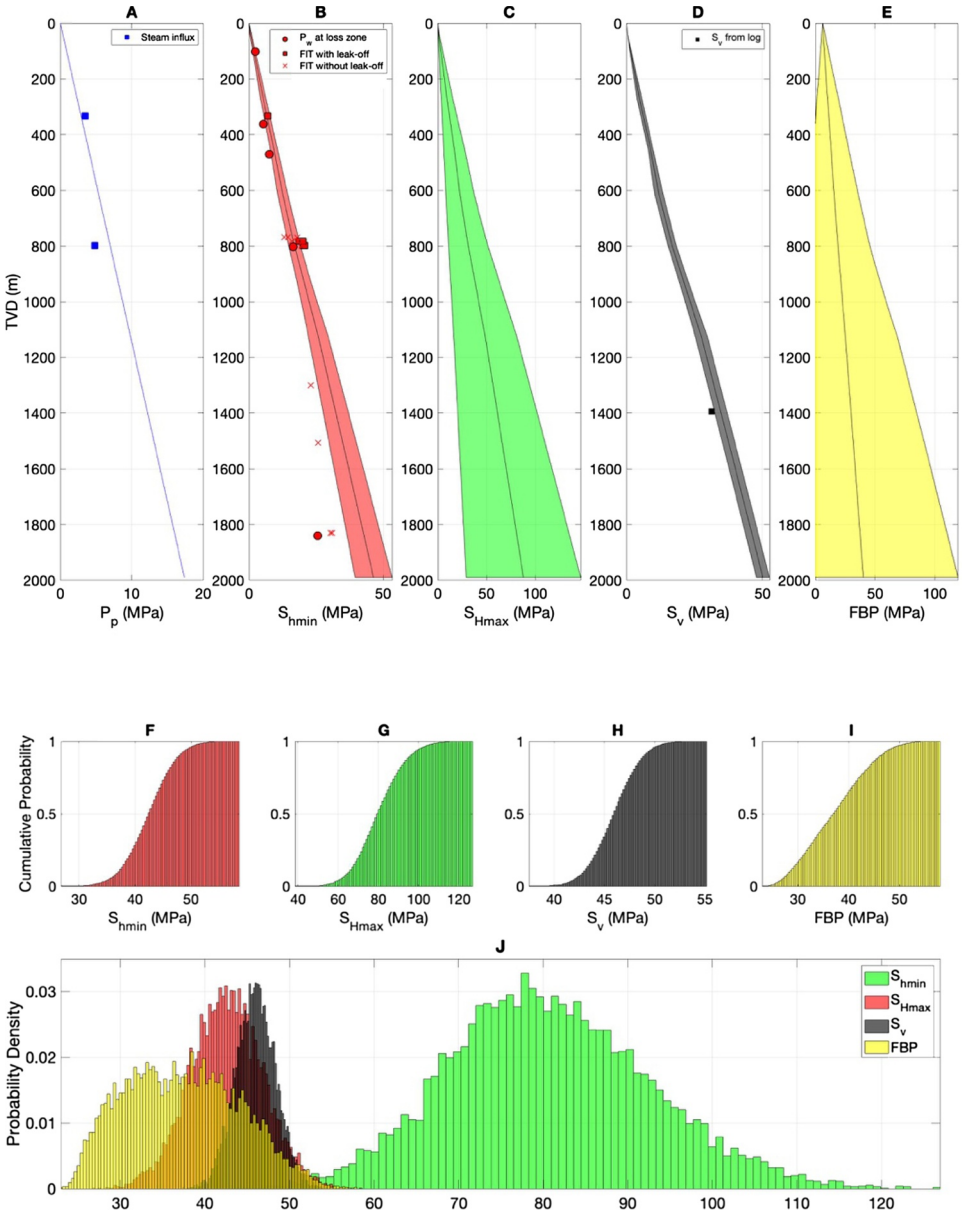

Fig. 9. Results of the MC simulations for the in-situ stress tensor and stimulation pressures in the Acoculco geothermal field (represented as mean stresses with standard deviations marked with the shaded area); A) P_p (blue boxes – discharge pressures during steam influxes); B) and F) S_{hmin} (red boxes – FIT's with leak-off, red stars – FIT's without leak-off, red circles – P_w at fluid loss zones); C) and G) S_{Hmax}; D) and H) S_v (black box – S_v from geophysical logging data recorded at the bottom of the logged interval); E) and I) *FBP*; J) superimposed frequency histogram of mean in-situ stress tensor and *FBP* at a depth of 1830 m.

with high (i.e., up to 1.28 g·cm^{-3}) drilling mud density. The rock matrix is impermeable, and most fractures are sealed. Hydraulic, thermal, and chemical stimulation treatments may be applied to overcome the near wellbore damage, open existing fractures, and connect the wells to nearby permeable fault damaged zones or fault intersections.

We mapped the NE- and NW-trending fault systems with surface expressions as close as 100 m to the EAC-1 and EAC-2 wells. Particularly young tilted sedimentary basin-fill indicates that these are active faults that may be open conduits at depth (Fig. 2). Whereas the mapped widths of these fault zones are typically less than 20 m, both outcrops close to the wells and examples elsewhere in the caldera indicate that mapped fault zones may locally be much wider areas of deformation (~100 m) that are mainly cemented with some open strands. However, none of the fluid losses in the EAC-1 and EAC-2 wells could be related to fault traces at the surface while only the deepest minor loss zone (~1839 – 1942 m) in the EAC-2 well coincides with an identified fault zone (~1828 – 1842 m). Instead, faults intersecting the wells seem to be closed by mineral precipitation. Nevertheless, the mapped surface structures may be potential stimulation targets and may also pose the risk of induced by fluid-injection seismicity.

The results of our analyses indicate that the stress regime is likely to be normal to strike-slip faulting. In both cases, the S_3 is horizontal, which would result in the development of vertical hydraulic fractures and preferential opening/stimulation of sub-vertical existing fractures as opposed to horizontal ones. The regional S_{Hmax} direction is estimated to strike NE-SW. The vertical hydraulic fractures would develop parallel to this direction. Thus, hydraulic fracture growth would be approximately parallel to the NE-striking normal faults and perpendicular to the NW-striking strike-slip faults identified near the wells. The same is true for hydraulically, chemically, or thermally stimulated existing fracture networks. However, no local data on present-day stress directions exist. Also, no vertical stress barriers were identified based on the available data. Thus, it remains unclear if and where fracture height growth would be restricted.

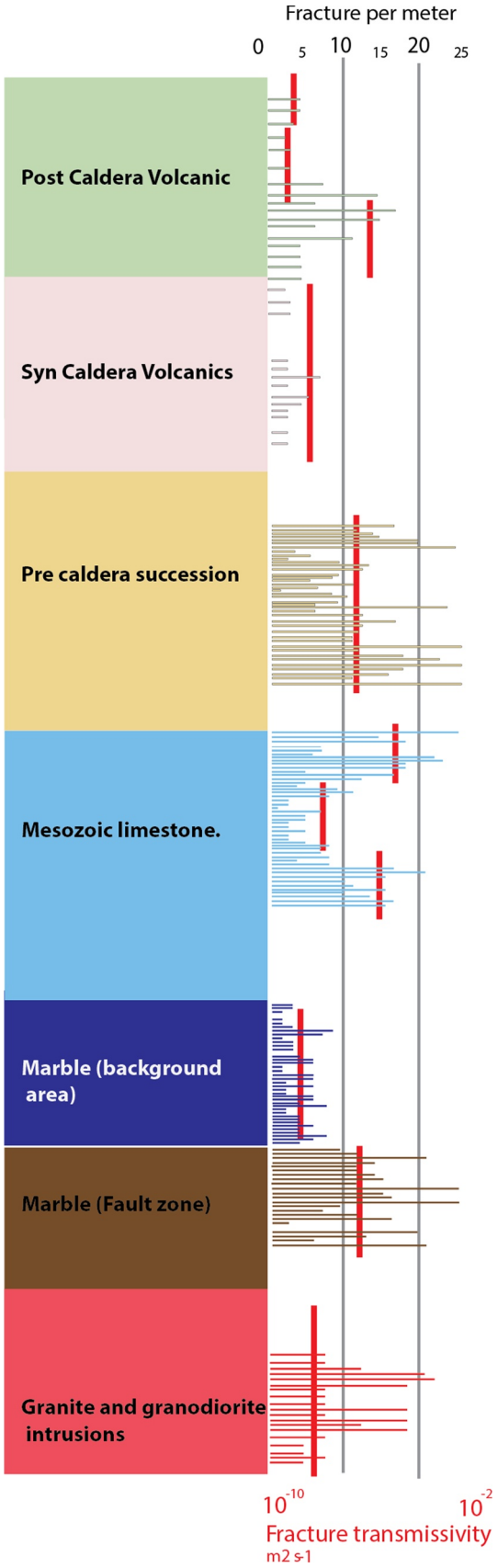

Fig. 10. A summary of a systematic mapping of fracture frequencies and inferred fracture transmissivities (fractures per meter) in analogue outcrops in the Acoculco, Los Humeros, and Las Minas areas. The dataset is represented as a pseudo well of the subsurface formations encountered in the EAC wells. The full dataset was presented in Bastesen et al. (2020) and Lepillier et al. (2020).

It is unlikely that both wells can be directly hydraulically connected by stimulation measures. This is because of the expected preferential stimulation of vertical fractures that makes it difficult to intersect vertical wells. This is also due to the presence of an oblique-slip transfer fault zone between the wells that strikes approximately perpendicular to the azimuth of S_{Hmax}. This indicates that this fault is likely to be less permeable compared to the perpendicular fault set if there has not been a recent slip. The steeply-dipping (65 – 80°) NE-trending normal faults, inferred to be active, are connected to the NW-trending oblique-slip transfer faults. These faults and fault intersections are potential stimulation targets for single wells and it may even be possible to connect the two wells hydraulically indirectly via these faults and associated fracture systems.

An important question of the EGS design is the geometry and filling characteristics of the pre-existing fractures. Fig. 10 shows the summary of a systematic mapping of fracture frequencies in nearby and regional outcrops displaying rock types equivalent to those encountered in the Acoculco wells. Fracture geometries mapped at the surface will not necessarily provide realistic permeabilities for the subsurface reservoir as burial history is significantly different. However, it will give a qualitative estimate of differences between fracture sets in different formations. One interesting example is shown for the faulted lava units ("old Volcanics"), which shows reasonably high fracture frequencies over large areas. In the EAC-2 well, one of the few fluid loss zones is encountered between 337 and 473 m depth in the Dacite unit, now hidden behind series of cemented casing strings, which is equivalent to one of the lava flow units in Fig. 10. The high fracture frequencies may be a result of a fault in this particular area or related to an interval with more open fractures. Marble shows overall moderate to low fracture frequencies in analogues; this is also the result reported from the analysis of the core samples from the EAC-1 well (Rocha et al., 2006). Skarn and limestone have high fracture frequencies in outcrops. Carbonate rocks are highly reactive to hot fluids and therefore fractures are likely to be sealed at reservoir levels by crystal growth and grain-boundary migration. Depending on the required temperatures, potential stimulation targets for the EAC-1 well are the calcite- and pyrite-filled fractures at ~850 m depth (i.e., skarn), the temperature anomaly at ~1650 m depth (i.e., marble), and/or fluid loss zones at 1736 m and 1909 – 1918 m. Potential stimulation targets for the EAC-2 well are the open fractures at ~1570 – 1900 m depth (i.e., skarn and marble) and in particular, the left lateral fault that was identified as fluid loss zone at ~1828 – 1842 m depth (i.e., granite). The full list of potential stimulation targets for both wells can be seen in Appendix C. The EAC-1 well should be considered as a primary candidate for carrying out a stimulation operation, due to its close vicinity to the both NW- and NE-striking fault systems.

Given the high temperature of the wells, long-term injection into the fluid-loss zones at low pressures, i.e., thermal stimulation treatments, is considered a viable option for both wells. Coldwater injection experiences from several wells in fractured rock in Iceland and New Zealand with similar temperatures show continuous permeability increase by as much as two orders of magnitude over several years (Grant et al., 2013). This permeability increase due to thermal contraction is reported to be more significant than the permeability increase caused by pressure changes in these wells (Grant et al., 2013). Laboratory experiments show that the permeability of granitic rocks can be improved significantly and permanently due to cooling. This process is more efficient the higher the temperature contrast is and the faster the cooling occurs (Siratovich et al., 2015).

To stimulate specific target intervals, zonal isolation is required. Due to the high temperatures, pre-existing fractures, and the enlarged well diameter, conventional zonal isolation by inflatable or swellable packers is risky and requires good quality televiewer logs. Therefore, it may be necessary to install and cement a liner above the top of the target zones. As this is a costly operation that additionally reduces the well diameter, it may be more feasible to perform long thermal

stimulation operations on the existing fluid loss zones either through the drill string or directly through an open hole. Another option would be to install a packer at the bottom of the production casing string to cut off cased and cemented sections of the wellbore from the threatening influence of stimulation conditions. Before any open hole stimulations, the integrity of the casing and cement sheath needs to be assured with borehole logging tools (Kruszewski et al., 2019). This is especially important for the case of EAC-1 and EAC-2 wells, which are already more than 25 and 12 years old, and cement or casing failure might have already developed since the last operations in the wellbore. During hydraulic and thermal stimulations, high-temperature differences, cyclical thermal loads or high pressures will be present. This may promote cement fracturing, cement debonding or casing failures. For the case of chemical stimulation, any direct contact of the cement sheath with the stimulation fluid should be prevented, as an aggressive stimulation fluid may lead to the rapid dissolution of the cement sheath. After the stimulation, a temperature log should be run to identify the depth of the stimulated zone. Once stimulation of a first well has been completed, identification of the stimulated zones, and confirmation of the stress field with leak-off tests and image logs, a third well may be drilled into the stimulated area to establish a geothermal doublet if no hydraulic connection between the two wells was achieved. This would require a high-resolution seismic monitoring network of sufficient location accuracy to be operating during stimulation. Despite the stimulation of existing wells, active (i.e., open and permeable) fault segments may be intersected by drilling towards NE-SW or NW-SE.

6. Conclusions

Based on the comprehensive analysis of geological, drilling, and geophysical logging data, we can conclude that the regional stress state is consistent with the geodynamics history and is in accordance with the stress indicators from the World Stress Map, where a dominant NW-trending crustal stretching direction (S_{Hmax} NE-trending) is indicated. The local stress regime depends on which shear zone is assumed as a stress marker since the area is characterized by the interplay and contemporaneous activity of right-lateral to oblique NW-striking fault zones and dominant NE-striking normal faults. Considering this context, the stress regime of the Acoculco geothermal area can be derived as in between normal ($S_v \geq S_{Hmax} \geq S_{hmin}$) and strike-slip ($S_{Hmax} \geq S_v \geq S_{hmin}$) faulting with NE-SW direction of S_{Hmax}, a linearized P_p gradient of 8.73 MPa·km^{-1}, an average linearized S_{hmin} gradient of 22.8 ± 3.3 MPa·km^{-1}, an average linearized S_v gradient of 24.3 ± 1.5 MPa·km^{-1}, and an average linearized S_{Hmax} gradient of 42.9 ± 28.5 MPa·km^{-1}. Due to the high uncertainties of S_{Hmax} gradient and *FBP*, it is advised to carry out additional caliper, image log, and (extended) leak-off tests to better constrain the in-situ stress tensor.

Potential EGS systems in the Acoculco geothermal field will rely on the fracture system and/or faults and not on the low permeability of the rock matrix. Based on the in-situ stress regime fluid-injection-induced and/or activated fractures and faults are likely to be (sub-)vertical and strike in the NE-SW direction. Potential faults between the two vertical wells (i.e., EAC-1 and EAC-2) and vertical fracture growth likely prevent the direct hydraulic connection between the wells. Hydraulic stimulation treatments may improve the productivity of individual wells by improving the permeability of existing structures intersecting the wellbore and/or hydraulic connection of the well to a permeable zone, such as a fault damage zone or fault intersections. If both wells can be connected to the same permeable structure a hydraulic connection may be possible. Thermal stimulation of existing inflow zones is considered to be the most promising stimulation method for both wells, especially in the deep granites.

Appendix A

Completion of the EAC-1 well

Drill bit diameter, cm	Casing outside diameter, cm	Steel grade	Casing weight, kg·m^{-1}	Casing setting depth, m	Type of casing
44.45	33.97	K-55	81.11	0 – 10	Surface

Funding

This work was carried out in the framework of the GEMex project, which received funding from the European Union's EU Horizon 2020 research and innovation program under Grant Agreement No 727550. The contribution of F.P. is funded by the Deutsche Forschungsgemeinschaft (DFG, German Research Foundation) – project number PA 3451/1-1.

Declaration of Competing Interest

The authors declare that they have no known competing financial interests or personal relationships that could have appeared to influence the work reported in this paper.

CRediT authorship contribution statement

Michal Kruszewski: Conceptualization, Methodology, Formal analysis, Investigation, Data curation, Writing - original draft, Writing - review & editing, Visualization. **Hannes Hofmann:** Conceptualization, Methodology, Formal analysis, Writing - original draft, Writing - review & editing. **Fidel Gomez Alvarez:** Investigation, Resources. **Caterina Bianco:** Investigation, Resources. **Adrian Jimenez Haro:** Investigation, Resources. **Victor Hugo Garduño:** Formal analysis, Investigation, Resources. **Domenico Liotta:** Formal analysis, Investigation, Resources, Data curation, Writing - original draft, Writing - review & editing. **Eugenio Trumpy:** Formal analysis, Investigation, Resources, Writing - original draft. **Andrea Brogi:** Investigation, Resources, Writing - review & editing. **Walter Wheeler:** Formal analysis, Investigation, Resources, Writing - original draft, Writing - review & editing. **Eivind Bastesen:** Formal analysis, Investigation, Resources, Writing - review & editing. **Francesco Parisio:** Conceptualization, Formal analysis, Writing - review & editing. **Erik H. Saenger:** Supervision, Project administration, Funding acquisition.

Declaration of Competing Interest

The authors report no declarations of interest.

Acknowledgments

This work is dedicated to the memory of Victor Hugo Garduño who prematurely passed away during the preparation of this manuscript. Victor Hugo contributed to the collection and interpretation of the field data here presented and introduced us to the Acoculco fieldwork with friendship and generosity. The authors would like to express great appreciation to CFE in Morelia for providing data from EAC-1 and EAC-2 wells. Authors would also like to thank Volker Wittig from Fraunhofer IEG, Lilibeth Morales, Marcela Sánchez Luviano, and Miguel Ramirez from CFE, Giordano Montegrossi from CNR, and Baptiste Lepillier from TU Delft for support during the preparation of this manuscript.

31.12	24.45	L-80	69.94	0 – 187.4	Anchor
21.59	17.78	N-80	55.06	0 – 800	Production
15.24	-	-	-	800 – 1500	Open hole
14.92	-	-	-	1500 – 2000	

Appendix B

Completion of the EAC-2 well

Drill bit diameter, cm	Casing outside diameter, cm	Steel grade	Casing weight, $kg \cdot m^{-1}$	Casing setting depth, m	Type of casing
44.45	33.97	K-55	81.10	0 – 9.52	Surface
31.12	24.45	L-80	69.94	0 – 200.08	Anchor
21.59	17.78	L-80	43.16	0 – 798.85	Production
14.92	-	-	-	798.85 – 1900	Open hole

Appendix C

Possible indications of fractures from both EAC-1 and EAC-2 wells

	EAC-1			EAC-2		
	Depth, m	Indicator	Reference	Depth, m	Indicator	Reference
Cased section	0 – 400	Thermal anomaly	Ramírez and García (2006)	0 – 400	Thermal anomaly	EAC-2 temperature profile
	70	Gas discharge	Gama et al. (1995)	102	Fluid loss	EAC-2 drilling report
	300 – 303	Fracture(s) filled with calcite	Gama et al. (1995)	333.2	Steam influx	EAC-2 drilling report
	600 – 603	Sealed fracture(s)	Gama et al. (1995)	337 – 388	Fluid loss	EAC-2 drilling report
				469 – 473	Fluid loss	EAC-2 drilling report
Open hole section	850 – 853	Fracture(s) filled with calcite and pyrite	Gama et al. (1995)	798.85	Steam influx	EAC-2 drilling report
				803	Fluid loss	EAC-2 drilling report
				1050	Thermal anomaly	EAC-2 temperature profile
	1250	Thermal anomaly	Pulido et al. (2010)	1300	Thermal anomaly	EAC-2 temperature profile
	1369	Fluid loss	Ramírez and García (2006)	1550	Thermal anomaly	EAC-2 temperature profile
	1650	Thermal anomaly	Pulido et al. (2010)	1520 – 1560	Sealed fracture(s)	Pulido et al. (2010)
	1736	Fluid loss	Ramírez and García (2006)	1570 – 1900	Open fracture(s) with epidotes	Pulido et al. (2010)
				1800	Thermal anomaly	EAC-2 temperature profile
				1828 – 1842	Fault filled with quartz, pyrite and epidote	Pulido et al. (2010)
				1834 – 1836	Intersection of two left-lateral faults	Pulido et al. (2010)
	1909 – 1918	Fluid loss	Ramírez and García (2006)	1839 – 1842	Fluid loss	EAC-2 drilling report

References

Amadei, B., Stephansson, O., 1997. Rock Stress and its Measurement. Chapman & Hall, London and New York.

Anderson, E.M., 1951. The Dynamics of Faulting and Dyke Formation with Applications to Britain. Oliver and Boyd, Edinburgh.

Angelier, J., 1979. Determination of the mean principal directions of stresses for a given fault population. Tectonophysics 56, 17–26.

Avellán, D.R., Macías, J.L., Layer, P.W., Cisneros, G., Sánchez-Núñez, J.M., Gómez-Vasconcelos, M.G., Pola, A., Sosa-Ceballos, G., García-Tenorio, F., Agustín, G.R., Osorio-Ocampo, S., García-Sánchez, L., Mendiola, I.F., Marti, J., López-Loera, H., Benowitz, J., 2019. Geology of the late Pliocene – Pleistocene Acoculco caldera complex, eastern Trans-Mexican Volcanic Belt (México). Journal of Maps 15 (2), 8–18. https://doi.org/10.1080/17445647.2018.1531075.

Barahim, A.A., Al-Akhaly, I.A., Shamsan, I.R., 2017. Engineering Properties of Volcanic Tuff from the Western Part of Yemen. SQU Journal for Science 22 (2), 81–88.

Bastesen, E., Wheeler, W., Torabi, A., Lepillier, B., Brogi, A., Liotta, D., Garduno, V.H., Garcia, O.H., Garcia, E.O., 2020. Geological structures and analogue permeability studies in Los Humeros and Acoculco geothermal systems. In: GEMex conference. Potsdam, GFZ. pp. 18–19 February.

Brudy, M., Zoback, M.D., Fuchs, K., Rummel, F., Baumgartner, J., 1997. Estimation of the complete stress tensor to 8 km depth in the KTB scientific drill holes: Implications for crustal strength. Journal of Geophysical Research 102 (B8), 18 1453 – 18,467, August 10.

Byerlee, J.D., 1978. Friction of rocks. Pure and Applied Geophysics 116, 615–626.

Calcagno, P., Evanno, G., Trumpy, E., Gutiérrez-Negrín, L.C., Macías, J.L., Carrasco-Núñez, G., Liotta, D., the GEMex T3.1 team, 2018. 3D preliminary geological models of Los Humeros and Acoculco geothermal fields (Mexico) – H2020 GEMex project. Advanced in Geosciences 45, 321–333. https://doi.org/10.5194/adgeo-45-321-2018.

Canet, C., Arana, L., González-Partida, E., Pi, T., Prol-Ledesma, R.M., Franco, S.I., Villanueva-Estrada, R.E., Camprubí, A., Ramírez-Silva, G., López-Hernández, A., 2010. A statistics-based method for the short-wave infrared spectral analysis of altered rocks: An example from the Acoculco Caldera. Eastern Trans-Mexican Volcanic Belt J. Geochem. Explor. 105, 1–10.

Canet, C., Hernández-Cruz, B., Jiménez-Franco, A., Pi, T., Peláez, B., Villanueva-Estrada, R.E., Alfonso, P., González-Partida, E., Salinas, S., 2015a. Combining ammonium mapping and short-wave infrared (SWIR) reflectance spectroscopy to constrain a model of hydrothermal alteration for the Acoculco geothermal zone, Eastern Mexico. Geothermics 53, 154–165.

Canet, C., Trillaud, F., Prol-Ledesma, R.M., González-Hernández, G., Peláez, B., Hernández-Cruz, B., Sánchez-Córdova, M.M., 2015b. Thermal history of the Acoculco geothermal system, eastern Mexico: Insights from numerical modeling and radiocarbon dating. Journal of Volcanology and Geothermal Research 305, 56–62.

Coates, G.R., Denoo, S.A., 1981. Mechanical properties program using borehole analysis and Mohr's circle. In: presented at the 1981 SPWLA 22nd Annual Logging Symposium. Houston. pp. 23–26 June.

Contreras, U., 2008. Evaluación del potencial Geotérmico del Proyecto de Acoculco, Puebla de acuerdo a los studios Geológicos, Geofísicos y geoquímicos. Departamento de Exploración report GG-ACO-01-08.

De la Cruz, M.V., Castillo-Hernández, D., 1986. Estudio geológico de la zona geotérmica de la caldera de Acoculco. CFE-GPG internal report 36/86, Puebla, pp. 23.
Demant, A., 1978. Características del Eje Neovolcánico Transmexicano y sus proble-mas de interpretación, Universidad Nacional Autónoma de México. Institutode Geología Revista 2, 172–187.
Dougherty, S.L., Clayton, R.W., 2014. Seismicity and structure in central Mexico: Evidence for a possible slab tear in the South Cocos plate. Journal of Geoph. Res. Solid Earth 119, 3424–3447.
Ego, F., Ansan, V., 2002. Why is the central trans-mexican volcanic belt (102Åã − 99ÅãW) in transtensive deformaHon? Tectonophysics 359, 189–208.
Ferrari, L., Orozco-Esquivel, T., Manea, V., Manea, M., 2012. The dynamic history of the Trans-Mexican Volcanic Belt and the Mexico subduction zone. Tectonophysics 522-523, 122–149.
Gama, R., Martínez, I., Cedillo, F., 1995. Reporte litológico-estructural megascópico de los núcleos cortados en el pozo exploratorio Acoculco N.1 ubicado en la porción Noroccidental del Estado de Puebla. CFE, Departmento de Exploración report No. DEX-AC-015/95.
García-Palomo, A., Macías, J.L., Jiménez, A., Tolson, G., Mena, M., Sánchez-Núñez, J.M., et al., 2018. NW-SE Pliocene-Quaternary extension in the Apan-Acoculco region, eastern Trans-Mexican Volcanic Belt. Journal of Volcanology and Geothermal Research 349, 240–255. https://doi.org/10.1016/j.jvolgeores.2017.11.005.
Gardner, G.H.F., Gardner, L.W., Gregory, A.R., 1974. Formation velocity and density - the diagnostic basics for stratigraphic traps. Geophysics 39, 770–780. https://doi.org/10.1190/1.1440465.
Gérard, A., Genter, A., Kohl, T., Lutz, P., Rose, P., Rummel, F., 2006. The deep EGS (Enhanced Geothermal System) project at Soultz-sous-Forêts (Alsace, France). Geothermics 35 (5–6), 473–483.
Gomez-Tuena, A., Orozco-Esquivel, M.T., Ferrari, L., 2005. Petrogenesis ignea de la Faja Volcanica Transmexicana. Boletín de la Sociedad Geológica Mexicana. Volumen Conmemorativo del Centenario 57. Temas Selectos de la Geología Mexicana, pp. 227–283.
Gómez-Tuena, A., Orozco-Esquivel, T., Ferrari, L., 2007. Igneous petrogenesis of the Trans-Mexican Volcanic Belt. In: In: Alaniz-Álvarez, S.A., Nieto-Samaniego, Á.F. (Eds.), Geology of México: Celebrating the Centenary of the Geological Society of México: Geological Society of America 422. Special Paper, pp. 1–53.
Grant, M.A., Clearwater, J., Quinao, J., Bixley, P.F., Le Brun, M., 2013. Thermal stimulation of geothermal wells: A review of field data. In: Proceedings, Thirty-Eight Workshop on Geothermal Reservoir Engineering. Stanford, California, February. pp. 11–13 SGP-TR-198.
Heidbach, O., Rajabi, M., Reiter, K., Ziegler, M., WSM Team, 2016. World stress map database release.
Jaeger, J.C., Cook, N.G.W., Zimmerman, R.W., 2016. Fundamentals of Rock Mechanics, 4th edition. Wiley-Blackwell.
Kallu, Raj, Roghanchi, P., 2015. Correlations between direct and indirect strength test methods. International Journal of Mining Science and Technology 25, 355–360.
Karaman, K., Cihangir, F., Ercikdi, B., Kesimal, A., Demirel, S., 2015. Utilization of the Brazilian test for estimating the uniaxial compressive strength and shear strength parameters. J. S. Afr. Inst. Min. Metall 115 (3) Johannesburg Mar.
Kruszewski, M., Montegrossi, G., Montes, M., Wittig, V., Gomez Garcia, A., Sánchez Luviano, M., Bracke, R., 2019. A wellbore cement sheath damage prediction model with the integration of acoustic wellbore measurements. Geothermics 80 (2019), 195–207.
Lajaunie, C., Courrioux, G., Manuel, L., 1997. Foliation fields and 3-D cartography in geology; principles of a method based on potential interpolation. Mathemat. Geol. 29, 571–584.
Lepillier, B., Bruhn, D., 2019. Las Minas Analogue Rocks characterization. Report for the GEMex project (unpublished).
Lepillier, B., Bruna, P.O., Bruhn, D., Bastesen, E., Daniilidis, A., Garcia, Ó., Torabi, A., Wheeler, W., 2020. From outcrop scanlines to discrete fracture networks, an integrative workflow. Journal of Structural Geology 103992.
López-Hernández, A., García-Estrada, G., Aguirre-Díaz, G., González-Partida, E., Palma-Guzmán, H., Quijano-León, J.L., 2009. Hydrothermal activity in the Tulancingo–Acoculco Caldera Complex, central Mexico: Exploratory studies. Geothermics 38 (3), 279–293 ISSN 0375-6505, 2009. MATLAB ver. R2018b.
McClure, M.W., Horne, N.R., 2014. An investigation of stimulation mechanisms in Enhanced Geothermal Systems. International Journal of Rock Mechanics & Mining Sciences 72, 242–260.
McKenzie, D.P., 1969. The relation between fault plane solution for earthquakes and the directions of the principal stresses. Bull. seism. Soc. Am. 59, 591–601.
Pasquare, G., Ferrari, L., Gardu, o-Monroy, V.H., Tibaldi, A., Vezzoli, L., 1991. Geologic map of the central sector of the Mexican Volcanic Belt, states of Guanajuato and Michoacan. Geological Society of America. Map and Chart Series MCH072.
Pasquarè, G., Garduno, V., Tibaldi, A., Ferrari, M., 1988. Stress pattern evolution in the central sector of the Mexican Volcanic Belt. Tectonophysics 146 (1-4), 353–364.
Pulido, C.L., Armenta, M.F., Silva, G.R., 2010. Characterization of the Acoculco Geothermal Zone as a HDR System. GRC Transactions 34.
Ramírez, M., García, J.M., 2006. Propuesta de caracterización del pozo exploratorio EAC-1 en la zona geotérmica de Acoculco. CFE Departamento de Ingeniería de Yacimientos report GPG, DINYAC-008-2006, Pue., México.
Rocha, S., Jiménez, E., Palma, H., 2006. Propuesta para dos pozos exploratorios en el proyecto geotérmico de Acoculco, Pue. CFE Departamento de Exploración report OGL-ACO-03/06.
Schlumberger, 2008. Reporte Tecnico, Pozo EAC-2, Intervalo: 803 - 1394 m.
Sippel, J., Scheck-Wenderoth, M., Reicherter, K., Mazur, S., 2009. Paleostress states at the south-western margin of the Central European Basin System e application of fault-slip analysis to unravel a polyphase deformation pattern. Tectonophysics 470 (1-2), 129–146.
Siratovich, P.A., Villeneuve, M.C., Cole, J.W., Kenedy, B.M., Bégué, F., 2015. Saturated heating and quenching of three crustal rocks and implications for thermal stimulation of permeability in geothermal reservoirs. Int. J. Rock Mech. Min. Sci. 80, 265–280.
Sosa-Ceballos, G., Macias, J.L., Avellán, D.R., Salazar-Hermenegildo, N., Boijseauneau-López, M.E., Pérez-Orozco, J.D., 2018. The Acoculco Caldera Complex magmas: Genesis, evolution and relation with the Acoculco geothermal system. Journal of Volcanology and Geothermal Research 358 (C), 288–306. https://doi.org/10.1016/j.jvolgeores.2018.06.002.
Suter, M., Lopez-MarHnez, M., Quintero-Legorreta, O., CasHllo MarHnez, M., 2001. Quaternary intra-arc extension in the central Trans-Mexican volcanic belt. GSA BulleHn 113 (6), 693–703.
Suter, M., 1991. State of stress and acHve deformaHon in Mexico and western Central America. The Geology of North America. Decade Map 1.
Torres, V., González, E., Birkle, P., 1995. Estudios petrográficos y de alteración hidrotermal de muestras de ripio y núcleos de pozos exploratorios en el campo geotérmico de las Derrumbadas-Acoculco. Informe interno del IIE/11/10184/F. 248, Puebla.
Weydt, L.M., 2019. Appendix A - 8.5 Rock property data lists. In: In: Bär, K., Weydt, L. (Eds.), Comprehensive report on the rock and fluid samples and their physical properties in the Acoculco and Los Humeros regions, Deliverable D6.1, WP6, GEMex H2020 project 1.5. European Comission, pp. 2019. 15-25. http://www.gemex-h2020.eu.
Weydt, L.M., Bär, K., Colombero, C., Comina, C., Deb, P., Lepillier, B., Mandrone, G., Milsch, H., Rochelle, C.A., Vagnon, F., Sass, I., 2018. Outcrop analogue study to determine reservoir properties of the Los Humeros and Acoculco geothermal fields, Mexico. Adv. Geosci. 45.
Zoback, M.D., 2007. Reservoir Geomechanics. Cambridge University Press.